

JVLGS: Joint Vision-Language Gas Leak Segmentation

Xinlong Zhao¹ Qixiang Pang² Shan Du¹ *

¹ University of British Columbia - Okanagan {xinlong.zhao, shan.du}@ubc.ca

² University of Central Missouri Qpang@ucmo.edu

Abstract

Gas leaks pose serious threats to human health and contribute significantly to atmospheric pollution, drawing increasing public concern. However, the lack of effective detection methods hampers timely and accurate identification of gas leaks. While some vision-based techniques leverage infrared videos for leak detection, the blurry and non-rigid nature of gas clouds often limits their effectiveness. To address these challenges, we propose a novel framework called Joint Vision-Language Gas leak Segmentation (JVLGS), which integrates the complementary strengths of visual and textual modalities to enhance gas leak representation and segmentation. Recognizing that gas leaks are sporadic and many video frames may contain no leak at all, our method incorporates a post-processing step to reduce false positives caused by noise and non-target objects—an issue that affects many existing approaches. Extensive experiments conducted across diverse scenarios show that JVLGS significantly outperforms state-of-the-art gas leak segmentation methods. We evaluate our model under both supervised and few-shot learning settings, and it consistently achieves strong performance in both, whereas competing methods tend to perform well in only one setting or poorly in both. We publish our code at: <https://github.com/GeekEagle/JVLGS>.

1. Introduction

Industrial gas leaks constitute critical emergencies that can lead to severe accidents. Methane contributes significantly to the greenhouse effect, while others like acetaldehyde are highly toxic [3]. Detecting these leaks is especially challenging because most industrial gases are colorless and odorless, making them imperceptible to the human senses. Traditional detection methods rely on electrochemical or photoionization sensors to monitor pipeline conditions [1, 53]. These approaches are hazardous because inspectors should place themselves near suspected leak points. To address these limitations, vision-based detection methods have gained increasing attention for their non-contact nature and potential for automation [38, 51].

*Corresponding author: Shan Du

These methods not only reduce labor costs but also eliminate direct exposure risks for inspectors [33]. Among these methods, video surveillance integrated with infrared (IR) imaging has shown strong potential for detecting gas leaks.

Nevertheless, video surveillance systems still face significant challenges. Even with infrared cameras, gas leaks are difficult to find, as they blend seamlessly into the backgrounds of frames. To address this issue, Lu et al [24] proposed a Gaussian-based method for background modeling to enable adaptive gas leak segmentation. However, its performance degrades significantly in the presence of irregular gas shapes and dynamic backgrounds. Similarly, optical flow-based methods [41, 49] are limited by the inconsistent shapes of gas and susceptible to noise interference.

Recent advances in deep learning have led to significant progress in camouflaged object detection (COD) tasks [43]. For instance, SINet-V2 [10] first outlined the rough contours of concealed objects. Wang et al [39], leveraging the YOLO series model [36], demonstrated strong performance in detecting visible, non-rigid objects like dust. GasSeg [52] integrated convolutional neural networks (CNNs) and Vision Transformers (ViT) [9] to develop a lightweight model for gas leak segmentation. However, its performance is limited by the inability to effectively capture motion cues from faint and ambiguous targets. While motion-based techniques offer a promising direction, long-term motion techniques [4, 6, 58] encounter difficulties due to the highly variable shapes of gas leaks and the lack of consistent features for the model to track over extended periods. In contrast, short-term approaches, such as RCRNet [48], leverage optical flow to capture motion characteristics. Nevertheless, both long-term and short-term methods remain susceptible to noise interference. Other recent work, such as SLT-Net [7] adopted implicit motion analysis and showed potential feasibility. However, it struggles to distinguish gas leaks from texturally similar objects, such as clouds. FGSTP [57] introduced fine-grained perception to refine motion information. However, the extracted motion features may not be reliably correlated with the actual target objects.

One potential approach to enhance the feature representation is to integrate temporal-spatial models with Vision-

Language Models (VLMs) [54]. CLIP [31] is one of the most well-known VLMs, employing a ViT as both its image and text encoder. However, its inference is too slow for real-time object segmentation. VisualBERT [21], designed for end-to-end vision-language correlation learning, offers flexibility but lacks specialization for spatially precise tasks. DALL-E [32] combines visual information with Large Language Models (LLMs) [56] to generate creative outputs, but it is not suited for accurate segmentation. OWLv2 [26] uses a ViT to process both image and text inputs by self-training, showing potential for open-vocabulary object detection. However, to the best of our knowledge, few existing methods effectively incorporate text-guided segmentation for blurry, non-rigid objects like gas leaks.

In this paper, we propose Joint Vision-Language Gas leak Segmentation (JVLGS), a novel framework designed to enhance model generalizability across diverse gas leak scenarios. Our method integrates text prompts between the vision encoder and motion extractor to enrich the information of the encoder. Following vision-language integration, the designed temporal-spatial module uses these enhanced features to analyze the motion and spatial cues of gas leaks. The decoder then integrates the multi-scale information through upsampling to generate the final masks. Many prior methods [7, 29, 57] are vulnerable to noise and minor movements in non-leak scenes, often producing false positives when no target is present. To address this, we incorporate a post-processing step to eliminate these false positives, ensuring entirely black masks for non-leak cases. We evaluate our model on two benchmark datasets under both supervised and few-shot learning settings to reflect realistic video surveillance use cases. Our main contributions are summarized as follows:

- We propose JVLGS, a model that integrates manually crafted text prompts with a video clip to enhance feature extraction. These prompts enable accurate localization and detection of gas leaks.
- We design a lightweight vision-language fusion approach, enabling more effective integration of visual features with textual representations.
- Our proposed model achieves significant performance gains in both supervised and few-shot learning, effectively simulating real-world leak detection scenarios.

2. Related Work

2.1. Gas Leak Detection and Segmentation

Traditional gas leak detection and segmentation methods rely on manual sampling and laboratory analysis using chemical reactions [2]. They are limited by slow response times, high labor costs, and risks associated with manual gas sampling [60]. Advancements in infrared thermography have emerged as a promising alternative, offering improved accuracy, broader detection coverage, and visualized

gas leaks. However, automatically segmenting invisible gas is still full of challenges. Existing methods can be categorized into image-based and video-based approaches. Image-based methods [11, 45, 50] rely on local features, such as shape and texture, but they often fail in blurry scenarios. In contrast, video-based methods [5, 19, 37] leverage the motion characteristics of gas in video sequences, resulting in improved accuracy. However, these methods often involve high computational costs and are not well-suited for real-time segmentation. To overcome these limitations, we propose a video-based segmentation network that achieves SOTA performance while maintaining the efficiency and scalability required for practical industrial applications.

2.2. Camouflaged Object Detection

Camouflaged Object Detection (COD) focuses on detecting objects that blend seamlessly into backgrounds. Traditional COD methods rely on hand-crafted features such as texture or color [12, 35]. However, these simple approaches often struggle in complex or low-resolution scenarios. Early deep learning methods leverage bio-inspired designs and attention mechanisms to enable efficient detection [18, 47]. Although these approaches achieve real-time detection, they struggle with detecting small or blurry objects. Additionally, motion-based methods incorporate cross-frame information and utilize motion coherence modules to achieve precise segmentation [14, 20, 44]. Their effectiveness is often reduced when background motion is unstable or when target objects exhibit minimal movement. End-to-end methods, which perform localization and segmentation within a unified model [16, 17, 55], leverage temporal continuity to maintain inter-frame consistency of target objects. In this paper, we propose an end-to-end framework to effectively address gas leak segmentation in complex and unstable scenarios.

2.3. Vision-Language Model

VLMs significantly improve the accuracy of vision-text matching by learning the correlations between visual and textual data [8, 54]. CLIP [31], a prominent VLM, extracts features from both visual and textual modalities and computes their similarity for one-to-one matching. However, obtaining high-quality image-text pairs is time-consuming and resource-intensive. CLIPSeg [25] adapts CLIP for pixel-level segmentation but may overlook low-contrast regions. GLIP [22] first detects objects and then refines predictions using text-guided attention. However, its high computational complexity can result in overfitting and reduced generalizability. OWLv2 [26] extends the text prompt capabilities of OWL-ViT [27] by incorporating self-training with pseudo-annotations. Its text model can match subtle semantic clues of leaks. In this paper, we leverage the pre-trained text model of OWLv2 as our text prompt module to construct a state-of-the-art gas leak segmentation model.

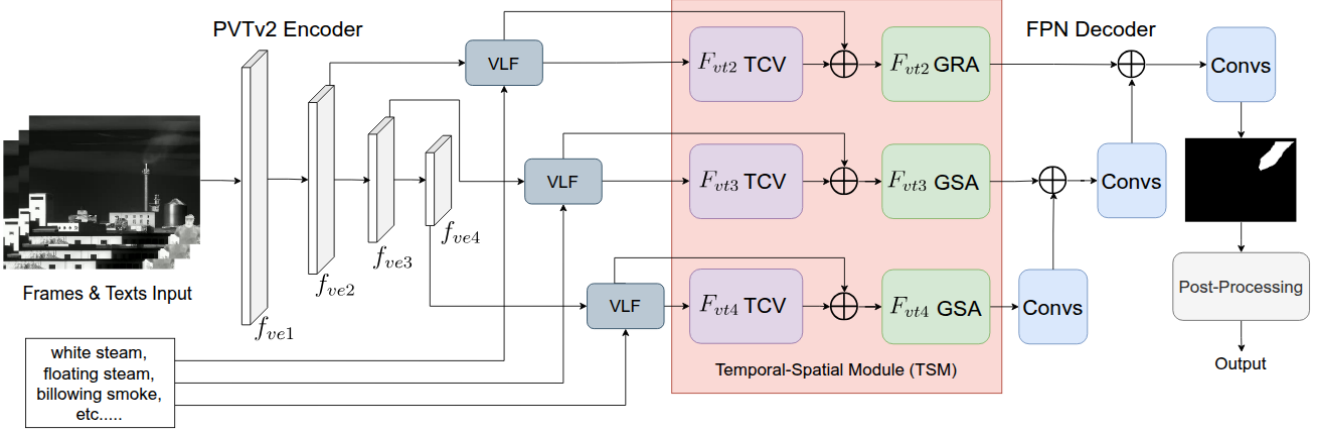


Figure 1. Framework of Joint Vision-Language Gas leak Segmentation (JVLGS). The inputs are video clips and text prompts of the target object. Visual and textual features are fused in the VLF module, followed by the Temporal-Spatial Module (TSM) and decoder. The post-processing removes false positives for final masks.

3. Method

3.1. Model Architecture

Figure 1 illustrates the architecture of our model, Joint Vision-Language Gas leak Segmentation (JVLGS). The model comprises the following components: (1) Vision encoders based on Pyramid Vision Transformer-v2 (PVTv2) [40]; (2) A Vision-Language Fusion (VLF) module designed to effectively integrate visual features with text representations; (3) A Temporal-Spatial Module (TSM) proposed to capture fine-grained motion and spatial information related to gas leaks; (4) An enhanced decoder built upon the Feature Pyramid Network (FPN) [23], optimized for multi-scale feature decoding; (5) A post-processing module to remove false positives. Overall, the model takes video clips and text prompts as inputs and outputs a binary mask for each frame.

Numerous studies have demonstrated that text prompts can help models capture rich semantic information, allowing them to distinguish target objects more effectively [15, 28, 46, 59]. Our proposed JVLGS incorporates vision and text features to segment target objects more accurately. Furthermore, we fine-tune the pretrained text model of OWLv2 [26] as our text module.

3.2. Vision-Language Fusion

The input video clips are first processed and divided by the vision encoder, PVTv2 [40] into three scale features $f_{ve}^i \in R^{C_v \times H/2^{i+1} \times W/2^{i+1}}$, $i \in \{2, 3, 4\}$, where C_v, H, W are channels, height and width of a frame. Figure 2 shows the details of the Vision-Language Fusion (VLF) module. The input of VLF, V_e , consists of f_{ve}^i , $i \in \{2, 3, 4\}$. The size of V_e is $T \times C_v \times H/2^{i+1} \times W/2^{i+1}$, $i \in \{2, 3, 4\}$, where T is the length of the video clip. The VLF firstly permute V_e to $V_e^T \in R^{T \times H/2^{i+1} \times W/2^{i+1} \times C_v}$, $i \in \{2, 3, 4\}$. Then V_e^T is linearly transformed to the vision feature f_v .

The text encoder is based on the OWLv2 text module, which employs a ViT backbone and was originally designed for zero-shot object detection [26]. Although OWLv2 outputs bounding boxes, we repurpose its textual representations to guide attention toward the target object, ultimately generating more precise binary masks. Therefore, we adopt the OWLv2 text encoder only for extracting textual representations, rather than using the full model. The VLF module is designed to integrate visual cues with textual guidance, where the vision features support the localization of target objects, and the text representations enrich visual features. Due to the variability in video content, a single prompt like “A Frame of Gas Leak” is insufficient for generalization across different videos. Thus, we introduce a diverse set of prompts, such as “White Steam” and “Billowing Smoke”, and we use a total of four prompt sequences during training. The effectiveness of each sequence is detailed in Appendix B. We denote the text input as $W \in R^{P_l \times d}$, where P_l is the number of the prompt sequence and d is the dimension of each prompt sequence. Then the prompted words are encoded by the text encoder as follows:

$$k, A = \text{TextEncoder}(W) \quad (1)$$

where k is the key of the prompt sequences, and A is an attention mask, indicating which tokens are correlated inputs for the text model. The k and A are then fed into the text encoder to obtain the textual representations as follows:

$$f_t = \text{TP}(\text{OwlText}(k, A)) \quad (2)$$

where $\text{OwlText}(k, A)$ represents the extracted text representations $f_t \in R^{P_l \times C_t}$, and C_t is the channel size of text representation. $\text{TP}(\cdot)$ denotes token-level pooling that selects a token from the hidden state of each sequence to refine f_t . Next, the text representation fuses with the f_v . The fusion operation in each scale is as follows:

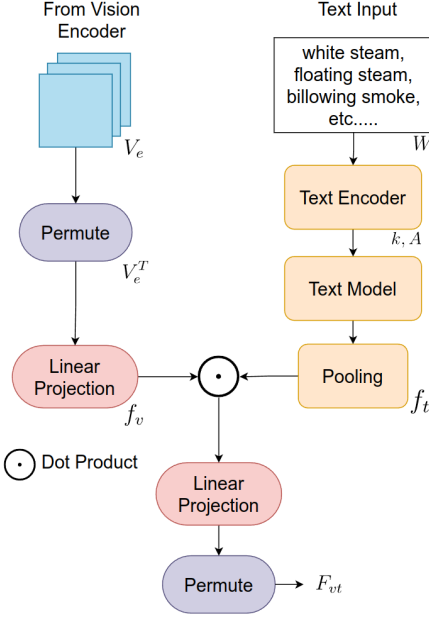


Figure 2. Architecture of the Vision-Language Fusion (VLF) module. Visual features are extracted by the vision encoder, while text prompts are manually provided by users.

$$F_{vt} = (\phi(f_v \cdot f_t))^T \quad (3)$$

where $\phi(\cdot)$ is the linear projection that converts the channel number of representative text C_t , to the channel number of vision features, C_v .

The resulting vision-language features, F_{vt} , is obtained by fusing the outputs of the vision and text encoders. After applying a linear projection to align feature dimensions, we fuse them through a dot product and then reshape the result to match the output shape of the vision encoder. The final fused feature, F_{vt} , is subsequently fed into TSM to capture motion and spatial information.

3.3. Temporal-Spatial Module

The Temporal-Spatial Module (TSM) is proposed to capture implicit motion information of the target object and refine it using the enhanced features produced by the Vision-Language Fusion (VLF) module. The architecture of TSM is illustrated in Figure 3. It consists of two key components: the Temporal Correlation Volume (TCV) and Granular Spatial Analysis (GSA).

The TCV is used to obtain strong motion features through the temporal correspondence, based on the combination of vision-text features in frames j and $j - 1$, $(F_{vt}^j, F_{vt}^{j-1}) \in R^{2C \times H' \times W'}$, where C is the channel number, H' and W' are height and width of the feature map. Inspired by [7], the TCV computes the correlation volumes between two feature maps of consecutive frames F_{vt}^j and F_{vt}^{j-1} to find subtle motion cues. The 4D correlation vol-

ume $CV(F_{vt}^j, F_{vt}^{j-1}) \in R^{H' \times W' \times H' \times W'}$, is as follows:

$$CV(F_{vt}^j, F_{vt}^{j-1})_{xyuv} = \exp \left(\sum_c (F_{vt}^j)_{xyc} \cdot (F_{vt}^{j-1})_{uvc} \right) \quad (4)$$

where c denotes the channel index, and $xyuv$ are coordinates of the current and adjacent frames. The $CV(F_{vt}^j, F_{vt}^{j-1})_{xyuv}$ denotes the correlation volumes between each element in F_{vt}^j and F_{vt}^{j-1} . For each feature map F_{vt}^j of a frame, the TCV computes two correlation volumes between current frame and two adjacent frames, $CV(F_{vt}^j, F_{vt}^{j-1})$ and $CV(F_{vt}^j, F_{vt}^{j+1})$, to strengthen the reliability of the extracted features.

Normalization is then applied to the last two dimensions of $CV(f_t, f_{t-1})_{xyuv}$, (u, v) , to refine the relevant motion features between reference frames and the current frame. The normalization is formulated as follows:

$$\widetilde{CV}(F_{vt}^j, F_{vt}^{j-1})_{xyuv} = \frac{CV(F_{vt}^j, F_{vt}^{j-1})_{xyuv}}{\sum_u \sum_v CV(F_{vt}^j, F_{vt}^{j-1})_{xyuv}} \quad (5)$$

Next, the normalized correlation volumes are aggregated with the channel-wise feature map $\lambda(F_{vt}^j, F_{vt}^{j-1}) \in R^{C \times H' \times W'}$, where $\lambda(\cdot)$ is a convolution layer that converts the channel number of (F_{vt}^j, F_{vt}^{j-1}) , $2C$ to C . At last, the TCV obtains the final correlation volume $\varphi(F_{vt}^{j-1,j})$. The calculation of another correlation volume $\varphi(F_{vt}^{j+1,j})$ is the same as $\varphi(F_{vt}^{j,j-1})$. The aggregation of the channel-wise features and normalized correlation volumes is as follows:

$$\varphi(F_{vt}^{j,j-1}) = \lambda(F_{vt}^j, F_{vt}^{j-1}) \cdot \widetilde{CV}(F_{vt}^j, F_{vt}^{j-1})_{xyuv} \quad (6)$$

While the TCV captures motion information, it lacks the ability to refine this into detailed spatial representations within each frame. To address this limitation, we propose a Granular Spatial Analysis (GSA) module to convert the extracted correlative motion into specific object features, inspired by [29]. The input of GSA $\tau(F_{vt}^{j,j-1})$ combines $(\varphi(F_{vt}^{j,j-1})$ and F_{vt}^j from VLF.

First, the 1×1 convolution expands the channel dimension of $\tau(F_{vt}^{j,j-1})$. Then the module divides the expanded $\tau(F_{vt}^{j,j-1})$ into g groups ($G_1 - G_g$) according to channels, and each group includes three channels of features $\rho_i^1, \rho_i^2, \rho_i^3$. Next, we split the first channel ρ_i^1 of G_i to concatenate it to the last two layers of the next group of features $(\rho_{i+1}^2, \rho_{i+1}^3)$. The overall processes are as follows:

$$\begin{aligned} \rho_i^1 &= \text{Split}(\text{Expand}(G_i)) \\ G_{i+1} &= \text{Concat}(G_{i+1}, \rho_i^1) \\ \rho_{i+1}^1 &= \text{Split}(\text{Expand}(G_{i+1})) \end{aligned} \quad (7)$$

The mixing is designed to analyze granular spatial cues across different channel groups, resulting in a more robust

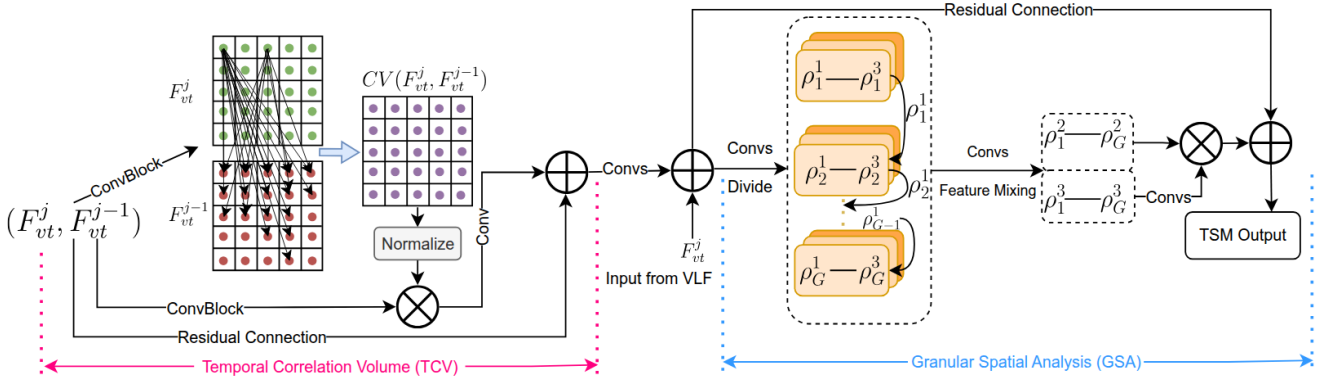


Figure 3. Framework of Temporal Spatial Module (TSM), which is constituted by two parts, Temporal Correlation Volume (TCV) and Granular Spatial Analysis (GSA). The former is to find the target object through inter-frame changing, while the latter refines the object features based on the TCV output.

and informative feature representation. Functionally, the iterative operation is equivalent to integrating a multi-path pyramid structure. Next, the second and third feature groups ($\rho_1^2 - \rho_G^2$ and $\rho_1^3 - \rho_G^3$) are merged into two new groups, N_2 and N_3 , respectively, through concatenation and convolution. Finally, the two sets of group-mixed features (N_2 and N_3) are fused through a convolutional block with a residual connection. The output of the GSA is denoted as gsa_{vt}^j .

$$N = N_2 \cdot N_3 \quad (8)$$

$$gsa_{vt}^j = \tau(F_{vt}^{j,j-1}) + Conv(N)$$

The TSM module effectively extracts valuable temporal and spatial cues across frames and channels, enabling rich information interaction and progressive feature refinement. This module strengthens the model’s ability to perceive the target object and provides a solid foundation for the final decoder predictions.

3.4. Decoder and Post-Processing

The decoder is a modified FPN that integrates multi-scale information by upsampling. Due to the strong features provided by the previous modules, the optimal choice for obtaining an accurate mask is the FPN module alone, rather than using the COD head as NCD does in [10], which can degrade the stability of the features. The effectiveness of our decoder design is further demonstrated in Section 4.4.

Unlike typical VOS studies, which assume that target objects are present in every frame of a video [4, 15, 59], gas leaks do not appear consistently throughout a video. Thus, the expected output of those non-leak frames should be completely black masks. However, significant noise results in false-positive masks for non-leak frames and makes many models fail in producing clean, completely black masks. To address the problem, we employ opening [34] as a post-processing. Opening is defined as the dilation of the erosion of a binary mask by a kernel. The effectiveness of

the opening depends on the kernel size. An oversized kernel may remove the true-positive part during the erosion stage, which cannot be recovered by the subsequent dilation. Conversely, a kernel that is too small may fail to eliminate false positives. We determine the optimal kernel size through an ablation study presented in Section 4.4. Overall, the post-processing effectively suppresses false positives while preserving the integrity of true leak regions.

3.5. Loss Function

In contrast to the previous study [7], which computes the loss by combining outputs from the inference frame and its adjacent frames, our approach calculates the loss solely based on the predicted mask and its corresponding ground truth (GT). Our loss function is applied exclusively to the predicted mask, avoiding multiple non-prediction outputs across scales, which would complicate training during backpropagation. We combine the weighted Binary Cross-Entropy (wBCE) L_{bce}^w and weighted Intersection over Union (wIoU) L_{iou}^w as our loss function, defined as follows:

$$L = L_{bce}^w + L_{iou}^w \quad (9)$$

where L_{bce}^w emphasizes pixels in vital regions such as object boundaries. These pixels are assigned higher weights to highlight their significance during training. Similarly, L_{iou}^w prioritizes the overlap computation in challenging regions, rather than treating all parts uniformly. Details of loss functions can be found in [42].

4. Experiments

4.1. Datasets

We evaluate our model on two datasets. The first, Sim-Gas, is a synthetic dataset created by [13]. Its backgrounds are partially sourced from the GasVid dataset [37], while the rest are generated using DALL·E 2 [32]. Manually labeling frames in GasVid is challenging due to the difficulty

Models	Input Type	Year	SimGas (Avg)			IGS-Few		
			$\mathcal{J} \uparrow$	$\mathcal{F} \uparrow$	$\mathcal{J} \& \mathcal{F} \uparrow$	$\mathcal{J} \uparrow$	$\mathcal{F} \uparrow$	$\mathcal{J} \& \mathcal{F} \uparrow$
SINet-V2 [10]	Image	2021	37.29	42.76	40.03	17.45	28.15	22.80
GasSeg [52]	Image	2024	37.35	46.16	41.76	55.40	67.00	61.20
SLT-Net [7]	Video	2022	39.24	44.40	41.82	66.43	76.52	71.47
Cutie [6]	Video	2024	-	-	-	46.61	59.07	52.84
Zoomnext [29]	Video	2024	21.67	27.10	24.39	59.28	70.43	64.86
LangGas [13]	Video	2025	53.57	63.95	58.76	10.66	15.16	12.91
FGSTP [57]	Video	2025	39.45	44.42	41.94	66.70	76.56	71.63
JVLGS (Ours)	Video	2025	61.73	70.25	65.99	67.06	77.05	72.05

Table 1. Quantitative comparison with benchmark methods on two datasets.

of precisely identifying leak areas. SimGas offers precise and controllable annotations, as the gas leak simulations are generated using Blender. Additionally, SimGas offers greater scenario diversity than GasVid, making it more representative of varied conditions. The dataset comprises 31 videos, totaling approximately 1,600 frames. Further details can be found in [13].

The second dataset is derived from the IGS dataset [52], which contains 4,453 images for training and 1,897 for testing. Since the training and testing frames originate from the same videos, we manually reorganize them into 27 distinct video sequences. In the original split [52], most frames from each video are used for training, with the remaining allocated for testing. However, video surveillance systems always adopt few-shot training, which uses a small number of frames per video for training, while the majority are reserved for testing. Thus, we follow the few-shot training strategy and cap the number of training frames per video at 30, while the hundreds of frames per video are for testing. We refer to this reconfigured dataset as IGS-Few.

4.2. Implementation Details

To ensure a consistent experimental environment and enable fair comparisons across methods, all experiments are conducted using the same software and hardware configurations. We set the experimental image resolution to 352×352 . Since the SimGas dataset does not have a predefined training–testing split, we adopt k-fold cross-validation to ensure the reliability of our evaluation. More information about our k-fold split is in Appendix F. We use the IGS-Few dataset, which is our modified split. Following standard practices in VOS evaluation, we adopt metrics that assess both region similarity and boundary accuracy between the predicted masks and the ground truth. Empirically, we adopt the Jaccard Index (\mathcal{J}), contour accuracy (\mathcal{F}), and their average ($\mathcal{J} \& \mathcal{F}$), as in [30], to evaluate mask overlap and boundary alignment. All experiments are conducted on an NVIDIA RTX 4090 GPU with 24 GB of memory. Further details are provided in Appendix A.

4.3. Results

4.3.1 Experimental Setup

When comparing our model with other SOTA methods, we observe significant variations in both the evaluation metrics and dataset splits used by different models. LangGas [13] computes \mathcal{J} and \mathcal{F} for each video by confusion matrices, while others calculate the average \mathcal{J} and \mathcal{F} scores in all frames of the test set. GasSeg [52] uses most frames for training and minors for testing, and it also averages background and foreground results in the metric evaluation. To ensure a fair comparison, we standardize the metric computation for all benchmark models. Additionally, we report results using each method’s original metric computation or dataset split when conducting individual comparisons.

4.3.2 Comparison with SOTA Methods

Table 1 summarizes the results using our unified metric computation. SINet-V2 [10] is an image-based early method for camouflaged object detection. It does not have a temporal module. Consequently, its performance is lower than many other methods on both datasets, 40.03 $\mathcal{J} \& \mathcal{F}$ on SimGas and 22.80 on IGS-Few. GasSeg [52] effectively finds leaks by fusing local and global information. It performs well on its proposed dataset, but it struggles on SimGas, resulting in a low $\mathcal{J} \& \mathcal{F}$ of 41.76. SLT-Net [7] and FGSTP [57] demonstrate comparable performance on both the SimGas and IGS-Few datasets. As video-based methods, they perform well when leaks are present in the video; however, they suffer from false positives in non-leak frames, often generating random artifacts. More information about the false positives is in Appendix D. ZoomNeXt [29] focuses on capturing multi-scale spatial features but overlooks motion information. Thus, it underperforms on the SimGas videos. Cutie [6] depends on the mask of the first frame to initialize the target object and guide segmentation in subsequent frames. The absence of leaks in the initial frames poses a huge obstruction to the SimGas dataset prediction. LangGas [13] is specifically designed for gas leak segmentation on their SimGas dataset. It combines back-

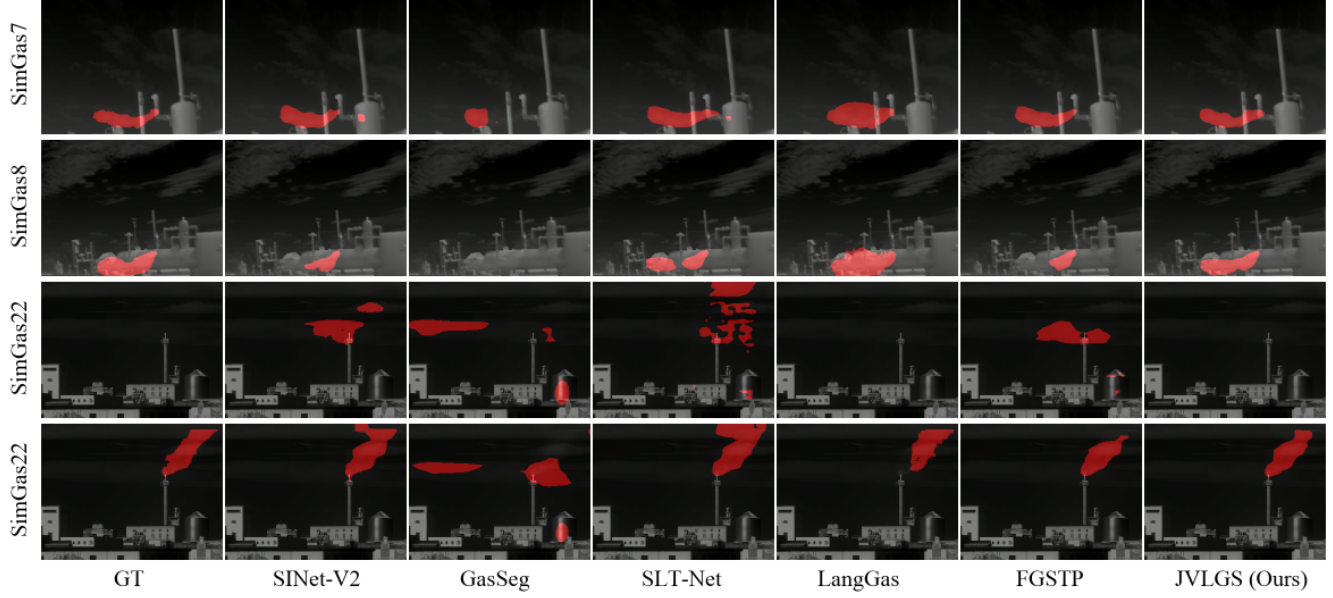


Figure 4. Visualized results on SimGas. Our model achieves the highest accuracy and generates whole-black masks for non-leak cases.

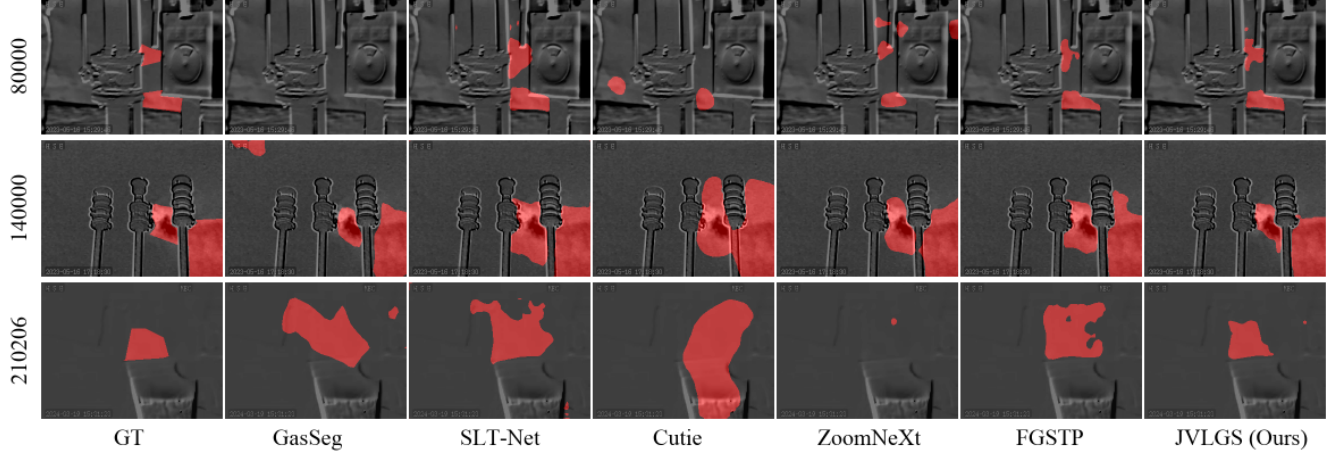


Figure 5. Visualized results on IGS-Few. Our model distinguishes the leak better than other models in few-shot learning.

ground subtraction with a large language model for mask prediction. But it struggles with the dithering backgrounds of the IGS-Few dataset, limiting its generalization ability. Our proposed method, JVLS, integrates motion, spatial, and textual prompts to enhance feature representation. It achieves a \mathcal{J} & \mathcal{F} score of 65.99 on SimGas and 72.05 on IGS-Few, outperforming all other methods on both datasets. Figures 4 and 5 present visualized results from each dataset, showcasing 1–2 frames from videos where the model performs particularly well. Further analysis is in Appendix C.

4.3.3 Different Metrics Comparison with Some Models

As noted in Section 4.3.1, LangGas and GasSeg use different evaluation metrics and dataset splits from ours. To ensure fairness, we re-implement their calculations to evaluate our method and LangGas. Table 2 presents results based on LangGas’s metric computation, while Table 3 shows per-

formance under GasSeg’s dataset split. In both settings, our method consistently outperforms the others, demonstrating its robustness across evaluation protocols.

Models	$\mathcal{J} \uparrow$	$\mathcal{F} \uparrow$	$\mathcal{J} \& \mathcal{F} \uparrow$
LangGas [13]	58.82	72.82	65.82
JVLS (Ours)	69.54	79.75	74.65

Table 2. Comparison with LangGas using its original metric calculation, on SimGas.

Models	$\mathcal{J} \uparrow$	$\mathcal{F} \uparrow$	$\mathcal{J} \& \mathcal{F} \uparrow$
GasSeg [52]	78.21	86.42	82.31
JVLS (Ours)	81.82	89.01	85.42

Table 3. Comparison with GasSeg using its original split, on IGS.

TSM	VLF	Decoder	Post-Processing	SimGas (Avg)			IGS-Few		
				$\mathcal{J} \uparrow$	$\mathcal{F} \uparrow$	$\mathcal{J} \& \mathcal{F} \uparrow$	$\mathcal{J} \uparrow$	$\mathcal{F} \uparrow$	$\mathcal{J} \& \mathcal{F} \uparrow$
✓		NCD		39.45	44.42	41.94	66.70	76.56	71.63
✓	✓	NCD		38.88	44.24	41.55	66.90	76.96	71.93
✓	✓	NCD	✓	57.73	66.05	61.90	66.94	76.97	71.95
✓		FPN	✓	59.21	67.26	63.23	66.97	77.08	72.03
✓	✓	FPN		39.06	44.50	41.78	67.02	77.05	72.03
✓	✓	FPN	✓	61.73	70.25	65.99	67.06	77.05	72.05

Table 4. Ablation studies on both datasets demonstrating the effectiveness of each component within our proposed model.

4.4. Ablation Studies

Table 4 presents the results of our ablation studies conducted on both the SimGas and IGS-Few datasets, using a consistent experimental setup based on our proposed model. We evaluate the individual contributions of the VLF module, FPN decoder, and post-processing.

Effectiveness of Text Prompts. We assess the impact of the language prompt module while keeping all other components unchanged. As shown in Rows 4 and 6 of Table 4, removing the VLF module results in segmentation degradation on both datasets, with a more noticeable drop on SimGas and a slight decrease on IGS-Few. This observation highlights the greater contribution of the VLF module on the SimGas dataset compared to IGS-Few.

Decoder Choice. The differences between Rows 2 and 5, as well as Rows 3 and 6 in Table 4, underscore the importance of decoder choice. Under identical conditions, regardless of the presence of the VLF module and post-processing, models using the FPN decoder consistently outperform those using the NCD decoder [57] on both datasets. This can be attributed to FPN’s straightforward multi-scale feature integration. In contrast, the NCD involves more complex structures, such as reversing and inserting feature maps, which may lead to incompatibilities with other modules and ultimately hinder overall performance.

Coordination Between Modules. An interesting observation from Table 4 is that Rows 1 and 2 appear to suggest a negative impact of the VLF module on the SimGas dataset. Even when the decoder is switched to FPN in Row 5, the performance remains lower than in Row 1, which uses the NCD decoder without VLF. This discrepancy can be attributed to interactions among components: the VLF module performs better when paired with the FPN decoder, as evidenced by the improvements between Rows 2 and 5, Rows 3 and 6. Notably, the combination of VLF, FPN, and post-processing in Row 6 achieves the highest scores on both datasets, underscoring the importance of effective coordination between modules.

Post-Processing Optimal Kernel Size. We also explore the optimal kernel size for the post-processing, with results shown in Figure 6. Both excessively small and large ker-

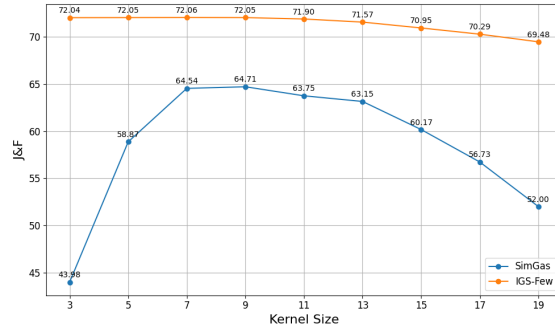


Figure 6. The relationship between $\mathcal{J} \& \mathcal{F}$ score and kernel size in our model. The blue line is $\mathcal{J} \& \mathcal{F}$ on the SimGas dataset, and the orange one is on the IGS-Few dataset.

nels degrade performance: small kernels fail to remove false positives, while large kernels tend to over-erode valid mask regions, making them unrecoverable during dilation. Our experiments identify a kernel size of 9 as delivering the best performance across both datasets, and we adopt this value as a hyperparameter in our model.

5. Conclusion

In this work, we present JVLGS, a novel framework designed for high-accuracy of gas leak segmentation. By integrating the complementary strengths of vision and text prompts, our method enhances feature representation and improves overall performance. Experimental results demonstrate that JVLGS achieves the best mask quality under both supervised and few-shot training. To mitigate false positives, we incorporate a post-processing module with an optimal kernel size, further improving reliability in non-leak scenarios. Our method provides a practical and effective solution for industrial gas leak detection and segmentation. Looking ahead, we plan to apply JVLGS to additional video datasets and investigate its potential for real-time decision-making in real-world deployments.

6. Acknowledgements

This work is supported by SSHRC under grant NFRF-GR024801.

References

- [1] Mutiu Adesina Adegbeye, Wai-Keung Fung, and Aditya Karnik. Recent advances in pipeline monitoring and oil leakage detection technologies: Principles and approaches. *Sensors*, 19(11), 2019. [1](#)
- [2] United States Environmental Protection Agency. Leak detection and repair compliance assistance guidance best practices guide - ldarguide.pdf, 2014. [2](#)
- [3] Diaa Badawi, Hongyi Pan, Sinan Cem Cetin, and A. Enis Çetin. Computationally efficient spatio-temporal dynamic texture recognition for volatile organic compound (voc) leakage detection in industrial plants. *IEEE Journal of Selected Topics in Signal Processing*, 14(4):676–687, 2020. [1](#)
- [4] Maksym Bekuzarov, Ariana Bermudez, Joon-Young Lee, and Hao Li. Xmem++: Production-level video segmentation from few annotated frames. In *Proceedings of the IEEE/CVF International Conference on Computer Vision (ICCV)*, pages 635–644, October 2023. [1, 5](#)
- [5] Yichao Cao, Qingfei Tang, and Xiaobo Lu. Stcnet: spatiotemporal cross network for industrial smoke detection. *Multimedia Tools and Applications*, 81(7):10261–10277, 2022. [2](#)
- [6] Ho Kei Cheng, Seoung Wug Oh, Brian Price, Joon-Young Lee, and Alexander Schwing. Putting the object back into video object segmentation. In *Proceedings of the IEEE/CVF Conference on Computer Vision and Pattern Recognition (CVPR)*, pages 3151–3161, June 2024. [1, 6](#)
- [7] Xuelian Cheng, Huan Xiong, Deng-Ping Fan, Yiran Zhong, Mehrtash Harandi, Tom Drummond, and Zongyuan Ge. Implicit motion handling for video camouflaged object detection. In *Proceedings of the IEEE/CVF Conference on Computer Vision and Pattern Recognition (CVPR)*, pages 13864–13873, June 2022. [1, 2, 4, 5, 6, 19](#)
- [8] Xiaoyi Dong, Jianmin Bao, Yinglin Zheng, Ting Zhang, Dongdong Chen, Hao Yang, Ming Zeng, Weiming Zhang, Lu Yuan, Dong Chen, Fang Wen, and Nenghai Yu. Maskclip: Masked self-distillation advances contrastive language-image pretraining, 2023. [2](#)
- [9] Alexey Dosovitskiy, Lucas Beyer, Alexander Kolesnikov, Dirk Weissenborn, Xiaohua Zhai, Thomas Unterthiner, Mostafa Dehghani, Matthias Minderer, Georg Heigold, Sylvain Gelly, et al. An image is worth 16x16 words: Transformers for image recognition at scale. *arXiv preprint arXiv:2010.11929*, 2020. [1](#)
- [10] Deng-Ping Fan, Ge-Peng Ji, Ming-Ming Cheng, and Ling Shao. Concealed object detection. *IEEE Transactions on Pattern Analysis and Machine Intelligence*, 44(10):6024–6042, 2021. [1, 5, 6, 12, 19](#)
- [11] Alessio Gagliardi and Sergio Saponara. Advised: Advanced video smoke detection for real-time measurements in antifire indoor and outdoor systems. *Energies*, 13(8):2098, 2020. [2](#)
- [12] Galun, Sharon, Basri, and Brandt. Texture segmentation by multiscale aggregation of filter responses and shape elements. In *Proceedings Ninth IEEE international conference on computer vision*, pages 716–723. IEEE, 2003. [2](#)
- [13] Wenqi Guo, Yiyang Du, and Shan Du. Langgas: Introducing language in selective zero-shot background subtraction for semi-transparent gas leak detection with a new dataset. *arXiv preprint arXiv:2503.02910*, 2025. [5, 6, 7, 19](#)
- [14] Chunming He, Kai Li, Yachao Zhang, Yulun Zhang, Zhenhua Guo, Xiu Li, Martin Danelljan, and Fisher Yu. Strategic preys make acute predators: Enhancing camouflaged object detectors by generating camouflaged objects. *arXiv preprint arXiv:2308.03166*, 2023. [2](#)
- [15] Shuting He and Henghui Ding. Decoupling static and hierarchical motion perception for referring video segmentation. In *Proceedings of the IEEE/CVF Conference on Computer Vision and Pattern Recognition*, pages 13332–13341, 2024. [3, 5](#)
- [16] Wenjun Hui, Zhenfeng Zhu, Guanghua Gu, Meiqin Liu, and Yao Zhao. Implicit-explicit motion learning for video camouflaged object detection. *IEEE Transactions on Multimedia*, 26:7188–7196, 2024. [2](#)
- [17] Wenjun Hui, Zhenfeng Zhu, Shuai Zheng, and Yao Zhao. Endow sam with keen eyes: Temporal-spatial prompt learning for video camouflaged object detection. In *Proceedings of the IEEE/CVF Conference on Computer Vision and Pattern Recognition*, pages 19058–19067, 2024. [2](#)
- [18] Ge-Peng Ji, Lei Zhu, Mingchen Zhuge, and Keren Fu. Fast camouflaged object detection via edge-based reversible recalibration network. *Pattern Recognition*, 123:108414, 2022. [2](#)
- [19] Alibek Kopbayev, Faisal Khan, Ming Yang, and Syeda Zohra Halim. Gas leakage detection using spatial and temporal neural network model. *Process Safety and Environmental Protection*, 160:968–975, 2022. [2](#)
- [20] Hala Lamdouar, Charig Yang, Weidi Xie, and Andrew Zisserman. Betrayed by motion: Camouflaged object discovery via motion segmentation. In *Proceedings of the Asian conference on computer vision*, 2020. [2](#)
- [21] Liunian Harold Li, Mark Yatskar, Da Yin, Cho-Jui Hsieh, and Kai-Wei Chang. Visualbert: A simple and performant baseline for vision and language. *arXiv preprint arXiv:1908.03557*, 2019. [2](#)
- [22] Liunian Harold Li, Pengchuan Zhang, Haotian Zhang, Jianwei Yang, Chunyuan Li, Yiwu Zhong, Lijuan Wang, Lu Yuan, Lei Zhang, Jenq-Neng Hwang, et al. Grounded language-image pre-training. In *Proceedings of the IEEE/CVF conference on computer vision and pattern recognition*, pages 10965–10975, 2022. [2](#)
- [23] Tsung-Yi Lin, Piotr Dollár, Ross Girshick, Kaiming He, Bharath Hariharan, and Serge Belongie. Feature pyramid networks for object detection, 2017. [3](#)
- [24] Quan Lu, Qin Li, Likun Hu, and Lifeng Huang. An effective low-contrast SF₆ gas leakage detection method for infrared imaging. *IEEE Transactions on Instrumentation and Measurement*, 70:1–9, 2021. [1](#)
- [25] Timo Lüdecke and Alexander Ecker. Image segmentation using text and image prompts. In *Proceedings of the IEEE/CVF conference on computer vision and pattern recognition*, pages 7086–7096, 2022. [2](#)

[26] Matthias Minderer, Alexey Gritsenko, and Neil Houlsby. Scaling open-vocabulary object detection. *Advances in Neural Information Processing Systems*, 36:72983–73007, 2023. [2](#), [3](#)

[27] Matthias Minderer, Alexey Gritsenko, Austin Stone, Maxim Neumann, Dirk Weissenborn, Alexey Dosovitskiy, Aravindh Mahendran, Anurag Arnab, Mostafa Dehghani, Zhuoran Shen, et al. Simple open-vocabulary object detection. In *European conference on computer vision*, pages 728–755. Springer, 2022. [2](#)

[28] Liangyang Ouyang, Ruicong Liu, Yifei Huang, Ryosuke Furuta, and Yoichi Sato. Actionvos: Actions as prompts for video object segmentation. pages 216–235, 2024. [3](#)

[29] Youwei Pang, Xiaoqi Zhao, Tian-Zhu Xiang, Lihe Zhang, and Huchuan Lu. Zoomnext: A unified collaborative pyramid network for camouflaged object detection. *IEEE Transactions on Pattern Analysis and Machine Intelligence*, 2024. [2](#), [4](#), [6](#), [19](#)

[30] Federico Perazzi, Jordi Pont-Tuset, Brian McWilliams, Luc Van Gool, Markus Gross, and Alexander Sorkine-Hornung. A benchmark dataset and evaluation methodology for video object segmentation. In *Proceedings of the IEEE conference on computer vision and pattern recognition*, pages 724–732, 2016. [6](#)

[31] Alec Radford, Jong Wook Kim, Chris Hallacy, Aditya Ramesh, Gabriel Goh, Sandhini Agarwal, Girish Sastry, Amanda Askell, Pamela Mishkin, Jack Clark, et al. Learning transferable visual models from natural language supervision. In *International conference on machine learning*, pages 8748–8763. PMLR, 2021. [2](#)

[32] Aditya Ramesh, Mikhail Pavlov, Gabriel Goh, Scott Gray, Chelsea Voss, Alec Radford, Mark Chen, and Ilya Sutskever. Zero-shot text-to-image generation. In *International conference on machine learning*, pages 8821–8831. Pmlr, 2021. [2](#), [5](#)

[33] Arvind P Ravikumar, Jingfan Wang, and Adam R Brandt. Are optical gas imaging technologies effective for methane leak detection? *Environmental science & technology*, 51(1):718–724, 2017. [1](#)

[34] Pierre Soille and Pierre Soille. Opening and closing. *Morphological image analysis: Principles and applications*, pages 105–137, 2004. [5](#)

[35] Ariel Tankus and Yechezkel Yeshurun. Detection of regions of interest and camouflage breaking by direct convexity estimation. In *Proceedings 1998 IEEE workshop on visual surveillance*, pages 42–48. IEEE, 1998. [2](#)

[36] Chien-Yao Wang, Alexey Bochkovskiy, and Hong-Yuan Mark Liao. Yolov7: Trainable bag-of-freebies sets new state-of-the-art for real-time object detectors. In *Proceedings of the IEEE/CVF Conference on Computer Vision and Pattern Recognition (CVPR)*, pages 7464–7475, June 2023. [1](#)

[37] Jingfan Wang, Jingwei Ji, Arvind P Ravikumar, Silvio Savarese, and Adam R Brandt. Videogasnet: Deep learning for natural gas methane leak classification using an infrared camera. *Energy*, 238:121516, 2022. [2](#), [5](#)

[38] Jingfan Wang, Lyne P. Tchapmi, Arvind P. Ravikumar, Mike McGuire, Clay S. Bell, Daniel Zimmerle, Silvio Savarese, and Adam R. Brandt. Machine vision for natural gas methane emissions detection using an infrared camera. *Applied Energy*, 257:113998, 2020. [1](#)

[39] Mingpu Wang, Gang Yao, Yang Yang, Yujia Sun, Meng Yan, and Rui Deng. Deep learning-based object detection for visible dust and prevention measures on construction sites. *Developments in the Built Environment*, 16:100245, 2023. [1](#)

[40] Wenhui Wang, Enze Xie, Xiang Li, Deng-Ping Fan, Kaitao Song, Ding Liang, Tong Lu, Ping Luo, and Ling Shao. Pvt v2: Improved baselines with pyramid vision transformer. *Computational visual media*, 8(3):415–424, 2022. [3](#), [12](#)

[41] Yakun Wang, Aiguo Wu, Jie Zhang, Meng Zhao, Wenshuai Li, and Na Dong. Fire smoke detection based on texture features and optical flow vector of contour. In *2016 12th World Congress on Intelligent Control and Automation (WCICA)*, pages 2879–2883, 2016. [1](#)

[42] Jun Wei, Shuhui Wang, and Qingming Huang. F³net: fusion, feedback and focus for salient object detection. In *Proceedings of the AAAI conference on artificial intelligence*, volume 34, pages 12321–12328, 2020. [5](#)

[43] Fengyang Xiao, Sujie Hu, Yuqi Shen, Chengyu Fang, Jinfa Huang, Chunming He, Longxiang Tang, Ziyun Yang, and Xiu Li. A survey of camouflaged object detection and beyond. *arXiv preprint arXiv:2408.14562*, 2024. [1](#)

[44] Junyu Xie, Weidi Xie, and Andrew Zisserman. Segmenting moving objects via an object-centric layered representation. In *Proceedings of the 36th International Conference on Neural Information Processing Systems, NIPS '22*, Red Hook, NY, USA, 2022. Curran Associates Inc. [2](#)

[45] Zhang Xu, Wang Wanguo, Li Xinrui, Liu Bin, and Tian Yuan. Flame and smoke detection in substation based on wavelet analysis and convolution neural network. In *Proceedings of the 2019 3rd International Conference on Innovation in Artificial Intelligence*, pages 248–252, 2019. [2](#)

[46] Cilin Yan, Haochen Wang, Shilin Yan, Xiaolong Jiang, Yao Hu, Guoliang Kang, Weidi Xie, and Efstratios Gavves. Visa: Reasoning video object segmentation via large language models. *arXiv preprint arXiv:2407.11325*, 2024. [3](#)

[47] Jinnan Yan, Trung-Nghia Le, Khanh-Duy Nguyen, Minh-Triet Tran, Thanh-Toan Do, and Tam V Nguyen. Mirrornet: Bio-inspired camouflaged object segmentation. *IEEE Access*, 9:43290–43300, 2021. [2](#)

[48] Pengxiang Yan, Guanbin Li, Yuan Xie, Zhen Li, Chuan Wang, Tianshui Chen, and Liang Lin. Semi-supervised video salient object detection using pseudo-labels. In *Proceedings of the IEEE International Conference on Computer Vision*, pages 7284–7293, 2019. [1](#)

[49] Charig Yang, Hala Lamdouar, Erika Lu, Andrew Zisserman, and Weidi Xie. Self-supervised video object segmentation by motion grouping. In *Proceedings of the IEEE/CVF International Conference on Computer Vision (ICCV)*, pages 7177–7188, October 2021. [1](#)

[50] Wei Ye, Jianhui Zhao, Song Wang, Yong Wang, Dengyi Zhang, and Zhiyong Yuan. Dynamic texture based smoke detection using surfacelet transform and hmt model. *Fire Safety Journal*, 73:91–101, 2015. [2](#)

[51] Shen Ying, Shao Kunming, Wu Jing, Huang Feng, and Guo Yuze. Optical gas detection: key technologies and applications review. *Opto-Electronic Engineering*, 47(4):190280–1, 2020. 1

[52] Huan Yu, Jin Wang, Zhan Wang, Jingru Yang, Kaixiang Huang, Guodong Lu, Fengtao Deng, and Yang Zhou. A lightweight network based on local-global feature fusion for real-time industrial invisible gas detection with infrared thermography. *Applied Soft Computing*, 152:111138, 2024. 1, 6, 7, 19

[53] Jie Yuan, Wenjing Mao, Chun Hu, Jianfeng Zheng, Dezhi Zheng, and Yunbo Yang. Leak detection and localization techniques in oil and gas pipeline: A bibliometric and systematic review. *Engineering Failure Analysis*, 146:107060, 2023. 1

[54] Jingyi Zhang, Jiaxing Huang, Sheng Jin, and Shijian Lu. Vision-language models for vision tasks: A survey. *IEEE Trans. Pattern Anal. Mach. Intell.*, 46(8):5625–5644, Aug. 2024. 2

[55] Xin Zhang, Tao Xiao, Ge-Peng Ji, Xuan Wu, Keren Fu, and Qijun Zhao. Explicit motion handling and interactive prompting for video camouflaged object detection. *Trans. Img. Proc.*, 34:2853–2866, May 2025. 2

[56] Wayne Xin Zhao, Kun Zhou, Junyi Li, Tianyi Tang, Xiaolei Wang, Yupeng Hou, Yingqian Min, Beichen Zhang, Junjie Zhang, Zican Dong, Yifan Du, Chen Yang, Yushuo Chen, Zhipeng Chen, Jinhao Jiang, Ruiyang Ren, Yifan Li, Xinyu Tang, Zikang Liu, Peiyu Liu, Jian-Yun Nie, and Ji-Rong Wen. A survey of large language models. *arXiv preprint arXiv:2303.18223*, 2023. 2

[57] Xinlong Zhao and Shan Du. Fine-grained spatial-temporal perception for gas leak segmentation. *arXiv: 2505.00295*, 2025. 1, 2, 6, 8, 19

[58] Junbao Zhou, Ziqi Pang, and Yu-Xiong Wang. Rmem: Restricted memory banks improve video object segmentation. In *Proceedings of the IEEE/CVF Conference on Computer Vision and Pattern Recognition (CVPR)*, pages 18602–18611, June 2024. 1

[59] Wenqi Zhu, Jiale Cao, Jin Xie, Shuangming Yang, and Yan-wei Pang. Clip-vis: Adapting clip for open-vocabulary video instance segmentation. *IEEE Trans. Cir. and Sys. for Video Technol.*, 35(2):1098–1110, Feb 2025. 3, 5

[60] Daniel Zimmerle, Timothy Vaughn, Clay Bell, Kristine Bennett, Parik Deshmukh, and Eben Thoma. Detection limits of optical gas imaging for natural gas leak detection in realistic controlled conditions. *Environmental Science & Technology*, 54(18):11506–11514, 2020. PMID: 32786569. 2

Appendix

A. Detailed Experimental Configuration

We use 5-fold cross-validation on SimGas dataset, where in each fold, 6 or 7 videos are sequentially selected for testing, and the remaining videos are used for training. This ensures that every video is included in the testing set. For all benchmark model experiments, the fold selections remain consistent to ensure fair and reproducible comparisons. For IGS-Few, we apply our own modified split to simulate the few-shot training, as described in Section 4.1. We use a batch size of 6. We train for 60 epochs on SimGas and 150 epochs on IGS-Few, since each dataset requires a different number of epochs to reach optimal performance. We set the initial learning rate (lr) to 10^{-4} , which decays to 10^{-5} in the final 20% of training epochs.

Model	SimGas			IGS-Few		
	$\mathcal{J} \uparrow$	$\mathcal{F} \uparrow$	$\mathcal{J} \& \mathcal{F} \uparrow$	$\mathcal{J} \uparrow$	$\mathcal{F} \uparrow$	$\mathcal{J} \& \mathcal{F} \uparrow$
Train from scratch	41.83	50.09	45.96	60.27	71.36	65.81
Pre-trained on COD10K	61.73	70.25	65.99	67.06	77.05	72.05

Table 5. Comparison between pretrained model and train-from-scratch model.

We adopt a pretrained encoder based on PVTv2 [40], which is hard to train from scratch because of its size and parameter count. Due to our limited computational resources and the lack of a large-scale gas-leak dataset, we leverage PVTv2 weights pretrained on the COD10K dataset [10]. Moreover, we compare the performances between training from scratch and pretraining on COD10K. As reported in Table 5, the encoder with pretrained parameters yields, on average, 26.53 % higher $\mathcal{J} \& \mathcal{F}$ score across the two datasets than training from scratch.

B. Analysis of Text Prompt Effect

We further verify the effectiveness of the language prompt. Specifically, we calculate the improvements of $\mathcal{J} \& \mathcal{F}$ by different prompts for each video on both datasets. Figures 7 and 8 illustrate the performance distribution across all prompts for both datasets. The vertical axes represent the number of videos, each displayed in a different color corresponding to a specific range of $\mathcal{J} \& \mathcal{F}$ values. We categorize the $\mathcal{J} \& \mathcal{F}$ values into five groups: red for 0–20 (lowest), orange for 20–40 (poor), yellow for 40–60 (moderate), light green for 60–80 (suboptimal), and green for 80–100 (best).

Figure 7 shows that the most influential prompt is “White Steam”, which significantly reduces the number of videos whose $\mathcal{J} \& \mathcal{F}$ scores are in the 0–20 range and shifts them into higher performance categories. Prompts like “Floating

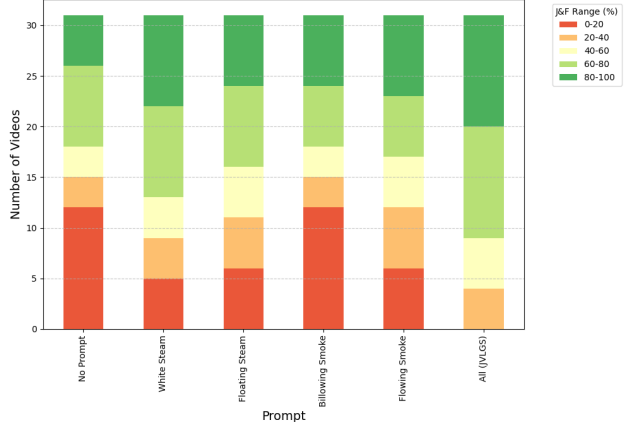


Figure 7. $\mathcal{J} \& \mathcal{F}$ value distributions of each prompt on SimGas dataset videos.

Steam” and “Flowing Smoke” also make notable contributions to the SimGas dataset. “Bellowing Smoke”, in particular, enhances performance on easier-to-segment videos, as evidenced by its longer deep green segment compared to the no-prompt baseline. However, the impact of text prompts on IGS-Few dataset is minimal, as shown in Figure 8. No single prompt leads to a noticeable performance improvement. Only the combined prompts result in a slightly enhanced performance. The limited effect on IGS-Few dataset can be attributed to the fact that few-shot learning has seen those scenarios during training, and text prompts become needless. Moreover, Figure 9 reveals that each prompt tends to benefit a specific subset of videos. The observation supports the use of multiple prompts during training. We achieve the best overall performance through the combination of different prompts.

Table 6 quantifies the contribution of each prompt on the SimGas dataset. We define prompt contribution as the average increase in $\mathcal{J} \& \mathcal{F}$ score relative to the non-prompt baseline, calculated across all videos. The column “Improved Videos” indicates the number of videos significantly influenced by each prompt. A video is considered “improved” if the improvement in its $\mathcal{J} \& \mathcal{F}$ score exceeds 0.5 points. The impact of each prompt is also visually illustrated in Figure 9.

Ultimately, all four prompt words work together to enhance features on the SimGas dataset, ensuring that each gas leak video benefits from at least one effective prompt. The last three Rows of Figure 9 show that the prompts have only a slight influence on predictions for the IGS-Few dataset. Thus, the language prompts are primarily beneficial for unseen scenarios. In contrast, the proposed model is ca-

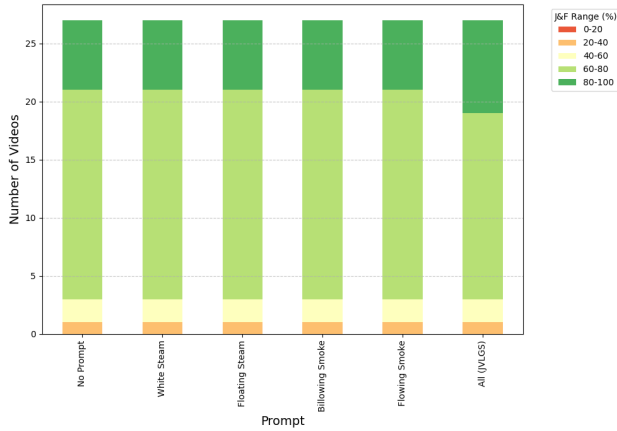


Figure 8. \mathcal{J} & \mathcal{F} value distributions of each prompt on IGS-Few dataset videos.

Prompts	Avg. \mathcal{J} & \mathcal{F} Contribution	No. of Improved Videos
No Prompt	0	0
“White Steam”	15.03	21
“Floating Steam”	10.26	12
“Billowing Smoke”	1.14	12
“Blowing Smoke”	8.17	18
All (JVLGS)	26.35	28

Table 6. Contribution of each prompt for JVLGS performance on the SimGas dataset.

pable of achieving reliable segmentation for seen scenarios even under few-shot training without additional language prompts.

C. Visualization of Results on SimGas and IGS-Few Datasets

Figure 10 presents the experimental results of the proposed model on the SimGas dataset. The qualities of model prediction in this dataset are similar in easy-segmentation videos like SimGas 7, 9, and 24 (Rows 1, 4, and 10). However, SLT-Net and FGSTP are significantly affected by noise in non-leak frames. Consider videos SimGas 9 and 22 (Rows 3 and 7) as examples. Neither of these frames contains a leak, yet the results from many models still produce foreground masks. In contrast, our JVLGS effectively removes these false positives, as shown in Rows 3 and 7. In more challenging cases, such as SimGas 19 and 21, the proposed model also shows superior performance. Video 19 contains clouds, whose visual properties are similar to gas leaks. Models like SINet-V2, GasSeg, and LangGas are notably misled by these clouds, while SLT-Net and FGSTP perform better but are still not as accurate as JVLGS. In Video 21, which simulates a chemical factory leak, the leakage is extremely subtle and can easily be mistaken for the

top of the chimney. JVLGS alone successfully segments the gas leak, guided by semantically relevant prompts. In summary, the integration of text prompts and effective post-processing enables JVLGS to generate more accurate masks while robustly suppressing noise.

The visualized results on the IGS-Few dataset are presented in Figure 11. Compared to SimGas, videos in IGS-Few have more challenging backgrounds, not only due to camera shake but also because of greater visual ambiguity between foreground and background. On this dataset, we train and test each model in a few-shot learning. GasSeg, the model proposed alongside the dataset, shows noticeably reduced performance in the few-shot learning compared to its original training split. It fails in many videos, such as 70000, 80000, 120000, and 130000. Similarly, models like ZoomNeXt (Column 5), which prioritize intra-frame features and lack motion modeling, underperform in subtle leak scenarios, like videos 80000, 120000, and 130000. Cutie, as a memory-based model, requires a mask from the first frame to guide segmentation. However, because of the non-rigid and emergent nature of gas leaks, monitoring them based on the initial mask proves ineffective. Among the motion-aware models, FGSTP (Column 6) outperforms SLT-Net (Column 2), largely due to its finer spatial perception. However, both models still struggle to capture accurate leak features in complex scenarios such as videos 90000, 120000, and 200000, where leaks emerge around valves, refueling pipelines, and test tubes, respectively. The proposed JVLGS, on Column 7, surpasses all benchmarks by the aforementioned innovations. This enables JVLGS to successfully handle multi-movement backgrounds and accurately segment leaks in challenging videos such as 120000, 130000, and 210206.

D. Failed Examples of SLT-Net and FGSTP in Non-leak Scenarios

Figure 12 illustrates the effectiveness of JVLGS in eliminating false positives. Previous methods (Rows 2–4) frequently produce false positives on non-leak frames. This often occurs when clouds are mistakenly identified as leaks, as seen in videos 20 and 22, due to their visual similarity. Even in non-cloud scenes, such as videos 7, 9, and 11, these methods incorrectly highlight the fluctuating luminance as objects. The size of non-leak masks is generally smaller than leak masks. Thus, the suitable size of kernel size would effectively erode non-leak foreground masks while preserving true leak regions. As shown in all examples in Figure 12, the result of our model does not have false positives on non-leak frames, successfully addressing the aforementioned challenges and focusing solely on accurate leak segmentation.

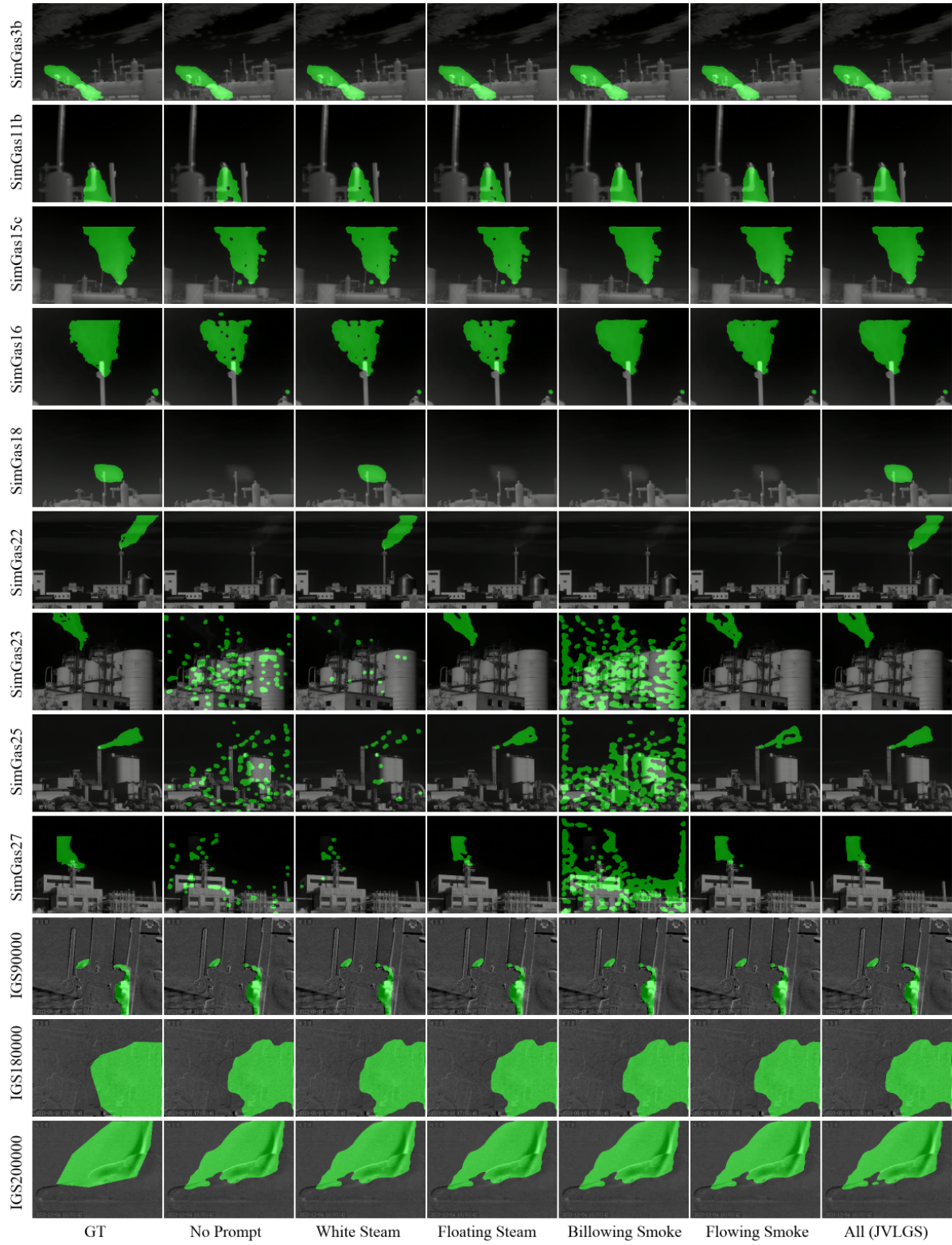


Figure 9. Visualized contribution of text prompt.

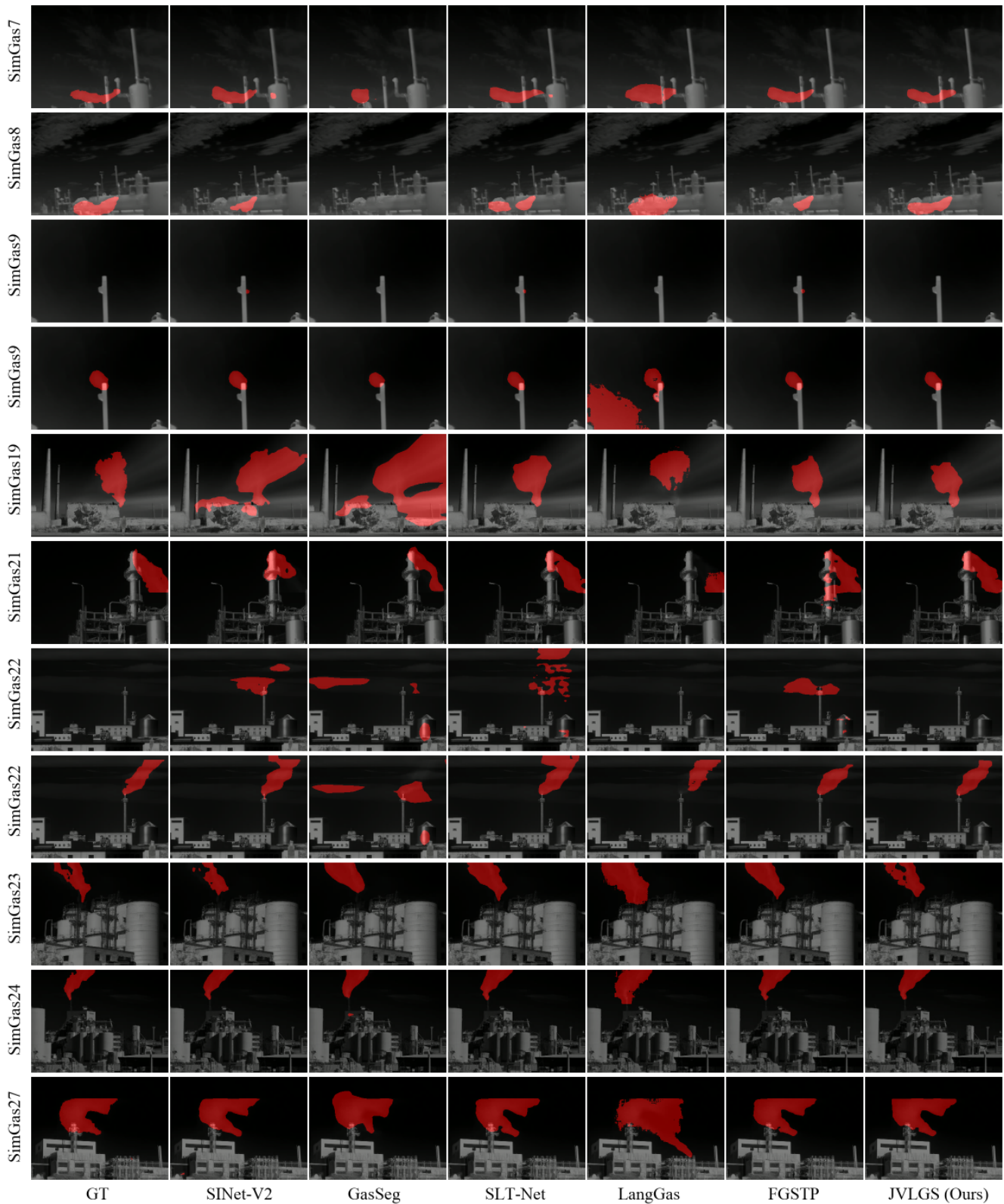


Figure 10. Visualized Results on SimGas dataset. Our model predicts more accurately than any other baseline model. And ours can give a whole black mask in non-leak condition.

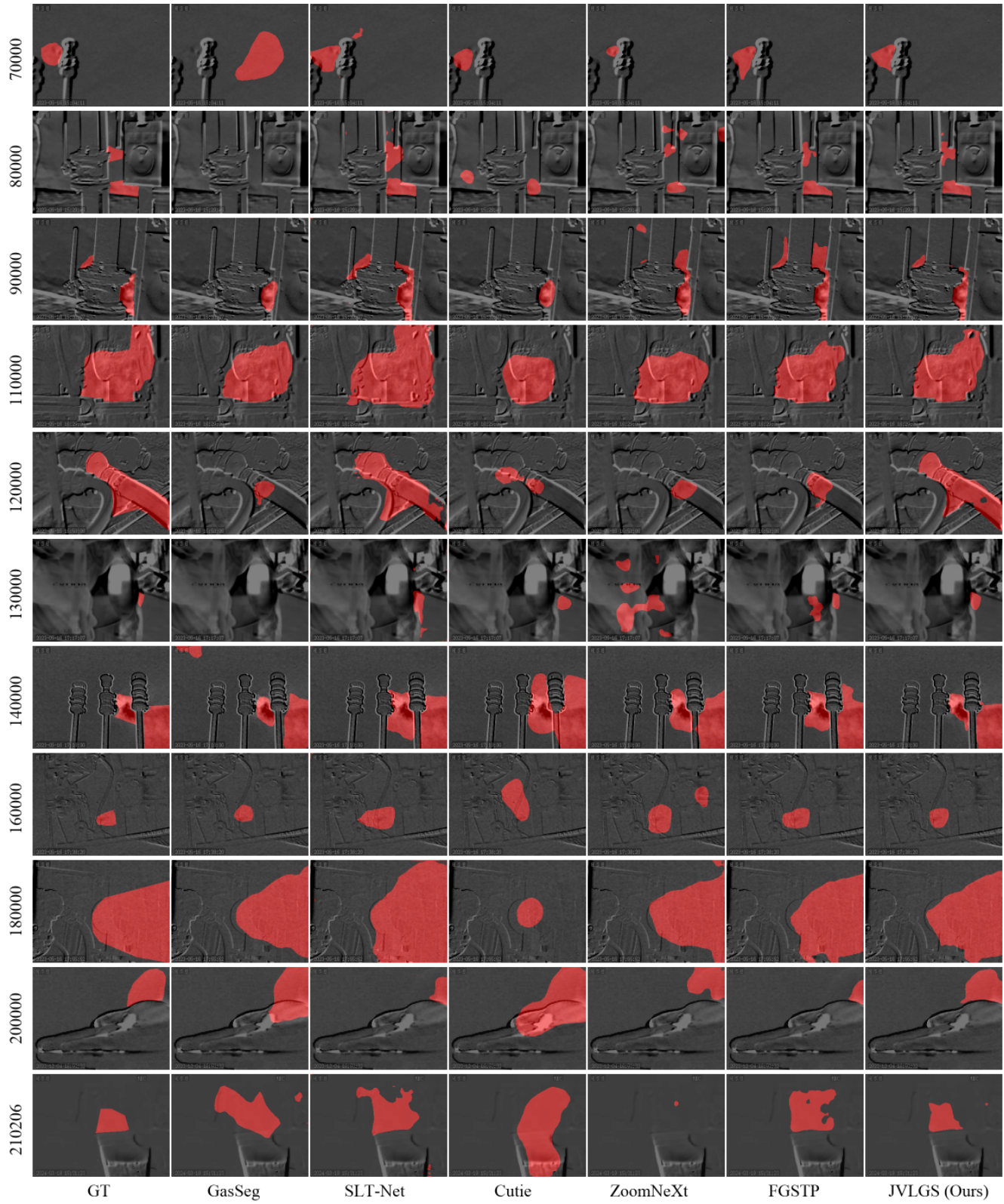


Figure 11. Visualized Results on IGS-Few dataset. Our model distinguishes the leak and background in various scenarios better than other models in few-shot learning.

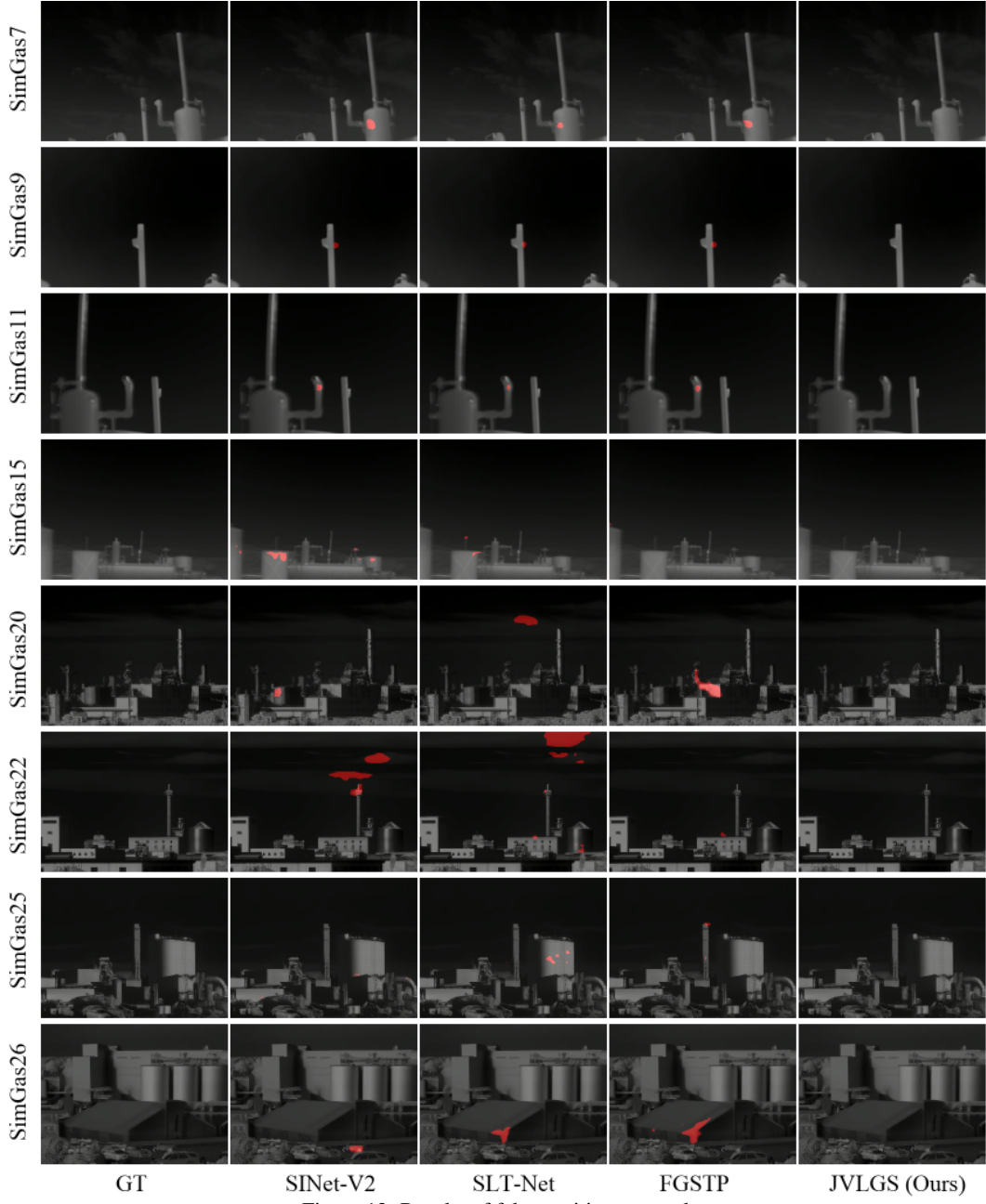


Figure 12. Results of false positive removal.

E. Performance-Efficiency Analysis

Figure 13 illustrates the trade-off between performance and efficiency across different models. Blue points represent results on the SimGas, red points represent results of IGS-Few, and green points are the average accuracy across both datasets. Ideally, a model should achieve high segmentation accuracy and fast inference speed, placing it in the upper right corner of the plot.

The JVLGS model achieves the best overall balance, delivering superior performance with only a minor reduction in inference speed. Among all models, the green point is

closest to the upper right corner, indicating the most favorable trade-off between accuracy and efficiency. While FGSTP, SLT-Net, and ZoomNeXt achieve similar or even faster speed on IGS-Few, the JVLGS model substantially outperforms them in average accuracy across both datasets.

F. Detailed Experimental Results on SimGas

Table 8 presents the detailed results of the model on the SimGas dataset. We adopt five-fold cross-validation, so we provide scores of the proposed metrics for each fold. The numbers reported in Table 1 are calculated using a weighted

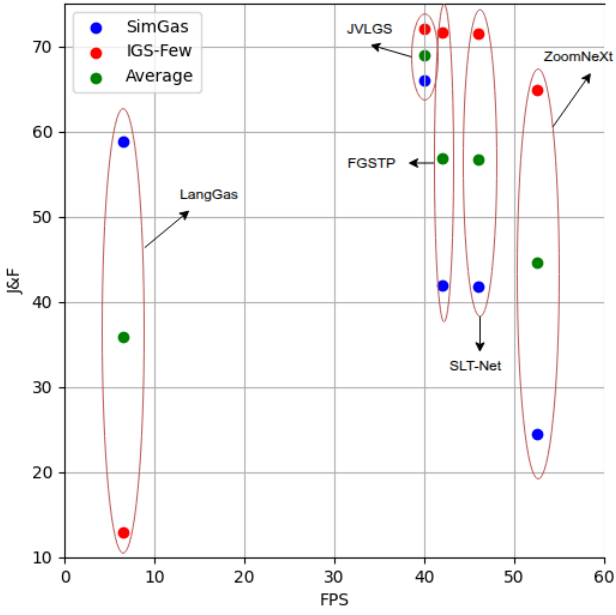


Figure 13. Performance-Efficiency Diagram.

average across all folds. The weight for each fold is determined by the total number of frames in its corresponding video group. Since the number of frames varies across videos and each fold consists of several grouped videos, the total number of frames differs between folds. As a result, each fold contributes a different weight to the overall performance evaluation based on its total frame count. Table 7 presents the weight assigned to each video group, calculated based on the total number of frames in that group.

		Fold Number	Weight	Videos Included	Frames Count
1	0.2603	1		1	451
		2		2	451
		2_human			451
		3		3	451
		3_bats			451
2	0.1856	4		4	451
		5		5	451
		6			450
		7			450
		8			451
3	0.1576	9		9	300
		10			300
		11			300
		11_brightbats			300
		12			551
4	0.2140	13			270
		15			270
		15_crowd			270
		16			250
		17			451
5	0.1825	18			551
		19			400
		20			393
		21			400
		22			400
		23			394
		24			370
		25			350
		26			350
		27			350
		28			400

Table 7. Weights of each fold on the SimGas dataset.

Models	Input Type	Year	Metrics	Fold 1	Fold 2	Fold 3	Fold 4	Fold 5
SINet-V2 [10]	Image	2021	\mathcal{J}	25.20	36.57	59.87	32.98	40.83
			\mathcal{F}	29.28	42.22	65.45	38.82	47.54
			$\mathcal{J}\&\mathcal{F}$	27.24	39.40	62.66	35.90	44.19
GasSeg [52]	Image	2024	\mathcal{J}	44.58	31.60	52.18	23.93	35.8
			\mathcal{F}	56.06	39.29	59.51	31.30	44.92
			$\mathcal{J}\&\mathcal{F}$	50.32	35.45	55.85	27.62	40.36
SLT-Net [7]	Video	2022	\mathcal{J}	29.37	38.81	58.04	37.05	40.07
			\mathcal{F}	33.65	44.52	63.62	42.38	45.39
			$\mathcal{J}\&\mathcal{F}$	31.51	41.67	60.83	39.72	42.73
ZoomNeXt [29]	Video	2024	\mathcal{J}	20.47	30.80	39.93	16.80	4.08
			\mathcal{F}	25.72	36.78	49.22	21.47	6.72
			$\mathcal{J}\&\mathcal{F}$	23.09	33.79	44.58	19.14	5.4
LangGas [13]	Video	2025	\mathcal{J}	55.37	52.16	62.46	53.00	45.47
			\mathcal{F}	66.22	61.23	71.84	63.76	56.87
			$\mathcal{J}\&\mathcal{F}$	60.80	56.70	67.15	58.38	51.17
FGSTP [57]	Video	2025	\mathcal{J}	29.77	37.67	59.05	37.14	40.84
			\mathcal{F}	33.70	43.41	64.43	42.64	45.54
			$\mathcal{J}\&\mathcal{F}$	31.74	40.54	61.74	39.89	43.19
JVLGS (Ours)	Video	2025	\mathcal{J}	63.94	54.08	72.91	60.33	58.34
			\mathcal{F}	72.84	62.21	79.31	69.23	68.10
			$\mathcal{J}\&\mathcal{F}$	68.39	58.14	76.11	64.78	63.22

Table 8. Values of Jaccard Index (\mathcal{J}), Contour Accuracy (\mathcal{F}), and Average ($\mathcal{J}\&\mathcal{F}$) for each fold of models' predictions on SimGas dataset.